Tailoring negative thermal expansion via tunable induced strain in La-Fe-Si-based multifunctional material

Rafael Oliveira Fleming, Sofia Gonçalves*, Amin Davarpanah, Iliya Radulov, Lukas Pfeuffer, Benedikt Beckmann, Konstantin Skokov, Yang Ren, Tianyi Li, John Evans, João Amaral, Rafael Almeida, Armandina Lopes, Gonçalo Oliveira, João Pedro Araújo, Arlete Apolinário, João Horta Belo⧫*

both authors contributed equally to this work
⧫ corresponding author e-mail: jbelo@fc.up.pt
R. O. Fleming*, S. Gonçalves*, A. Lopes, G. Oliveira, R. Almeida, J. P. Araújo, A. Apolinário and J. H. Belo⧫
Institute of Physics of Advanced Materials, Nanotechnology and Nanophotonics (IFIMUP), Departamento de Física e Astronomia da Faculdade de Ciências da Universidade do Porto, Rua do Campo Alegre, 687, 4169-007 Porto, Portugal

A. Davarpanah, I. Radulov, L. Pfeuffer, B. Beckmann, K. Skokov,
Institute of Material Science, Technical University of Darmstadt, 64287 Darmstadt, Germany

Y. Ren
Department of Physics, City University of Hong Kong, Kowloon, Hong Kong, China

T. Y. Li
X-ray Science Division, Argonne National Laboratory, Lemont, IL 60439, USA

A. Davarpanah, J. Amaral
Department of Physics and CICECO, University of Aveiro, Universitary Campus of Santiago, 3810-193 Aveiro, Portugal

J. S. O. Evans
Department of Chemistry, Durham University, South Road, Durham DH1 3LE, United Kingdom

Keywords: ((3–7 keywords, not capitalised, plural, separated by commas, no full stop))
negative thermal expansion, strain, microstructuring, phase transitions, magnetocaloric materials, multifunctional materials

0. Abstract

Zero thermal expansion (ZTE) composites are typically designed by combining positive (PTE) with negative thermal expansion (NTE) materials acting as compensators and have many diverse applications, including in high-precision instrumentation and biomedical devices. $La(Fe_{1-x},Si_x)13$-based compounds display several remarkable properties, such as giant magnetocaloric effect and very large NTE at room-temperature. Both are linked via strong magnetovolume coupling, which leads to sharp magnetic and volume changes occurring simultaneously across first-order phase transitions; the abrupt nature of these changes makes them unsuitable as thermal expansion compensators. To make these materials more useful practically, the mechanisms controlling the temperature over which this transition occurs and the magnitude of contraction need to be controlled. In this work, ball-milling was used to decrease particles and crystallite sizes and increase the strain in $LaFe_{11.9}Mn_{0.27}Si_{1.29}H_x$ alloys. Such size and strain tuning effectively broadened the temperature over which this transition occurs. The material's NTE operational temperature window was expanded, and its peak was suppressed by up to 85%. This work demonstrates that induced strain is the key mechanism controlling these materials' phase transitions. This allows the optimization of their thermal expansion towards room-temperature ZTE-applications.

1. Introduction

Currently, there is an urge to mechanically control materials at the micro and nanoscale in a wide set of technological industries e. g. micro-devices, large telescopes, dentistry, sensors, and fuel cells [1-7]. Small mechanical distortions originating from materials' thermal expansion can degrade high-precision devices and instruments, making the accurate control of materials' and devices' thermal expansion of fundamental interest. This issue is particularly problematic for devices with several constituents (such as multilayered devices) where there is likely to be a thermal expansion mismatch between their constituent materials [3,4,7-9]. Such thermal expansion mismatch between materials can cause mechanical cracks and disrupted electrical connections. In such cases, controllable thermal expansion can enhance device reliability and prolong their lifetime. [4-6,8]. In order to tackle this technological problem, materials and/or

composites with near-zero thermal expansion behaviour (zero thermal expansion (ZTE) or invar materials) are required [5,7,9].

While most materials expand when heated, exhibiting a positive thermal expansion (PTE), some possess an unusual property of volume contraction - these are said to have a negative thermal expansion (NTE) [1-5,8,10]. Functional composites' thermal expansion can be tailored by combining PTE with NTE constituent materials. In particular, ZTE composites can be achieved by combining materials with isotropic thermal expansions, where the NTE material will act as a thermal expansion compensator [5,7,11-13]. Therefore, it is extremely important to understand the underlying intrinsic chemical-physical behaviour of these NTE materials and provide fundamental insight so that they are controllable for a wide range of applications [14-28].

Among the different mechanisms that lead to NTE behaviour [1-5,8,10], one is the occurrence of a magnetovolume coupling [17,29-32]. This mechanism typically arises from a simultaneous magnetic and atomic lattice transition, where the large magnetization variation at the Curie temperature (T_C) is accompanied by a large change in the crystal structure. The simultaneous variation of two order parameters (magnetization and unit cell volume) typically occurs in materials with first-order phase transitions such as the LaFeSi, HfNbFe and MnZnN material families [4,5]. This coupling provides the ability to tune the thermal expansion of these materials by adjusting their magnetic properties.

More recently, another mechanism controlling the thermal expansion has been attracting research attention: the size confinement of any given material (typically when one of the spatial dimensions is smaller than 100 nm) of any given material. Such microstructural downsizing can lead to the appearance of novel physical properties due to size-induced effects [13,16]. In particular, several materials that present bulk PTE have been found to exhibit NTE when presenting at least one dimension confined at the nanoscale [2,13,16,19,33]. These materials' properties, such as magnetization, superficial/interfacial coordination, local lattice symmetry, and elemental distribution, can be changed through size reduction, enabling the possibility of tailoring associated features such as their thermal expansion. [13,16].

The La(Fe$_{1-x}$,Si$_x$)$_{13}$-derived compounds are very well known for their giant magnetocaloric effect and NTE behaviour [9,10,14,15,17,18,34-46]. Their crystal structure is cubic with *Fm-3c* space group, and they display a ferromagnetic-to-paramagnetic (FM-PM) isostructural transition, corresponding to a low-temperature high-magnetization (ordered) state which evolves into a high-temperature low-magnetization (disordered) state, as the temperature is increased across their T_C [26]. Along these transitions, the crystal structure is retained, but the

unit cell volume contracts by 3000-30000 ppm typically over a < 50K temperature interval [5,9,15,35-37]. To act as compensators, NTE materials should have a more gradual change of volume over a larger temperature window, akin to the typical changes on standard PTE materials. Fortunately, it is possible to tune and shape the profile of the magnetization versus temperature curves (namely the T_C and the dM/dT) by tuning both extrinsic (pressure, magnetic field) [35,42-46] and intrinsic (stoichiometry) properties [9,10,18,35,38-41]. Recently, there have been remarkable examples of thermal expansion control via chemical substitutions, where the typically abrupt NTE behaviour is smoothed across a wider temperature window [9,10,18,35,38-41]. For example, by replacing Fe by Co and Mn, or by adjusting the Si/Fe ratio, or even by electrolytic hydrogenating La-Fe-Si, Li's group has successfully been able to tune the operational temperature and smooth out La-Fe-Si sharp volume transition [9,15,24-26].

This work proposes an alternative mechanism to control the thermal expansion of strongly magnetovolume coupled materials - microstructural strain induced by ball-milling (BM) [47,48]. It is known that magnetic disorder (which can be induced by microstrutural strain) has a strong impact on the magnetic transition profile: increasing magnetic disorder leads to a broadening of the magnetic transition which is associated with a wider temperature distribution of Tc´s [47, 48, 56, 59]. Hence, due to La-Fe-Si strong magnetovolume coupling, in this work we propose to make use of the microstrutural strain to control the magnetic transition profile and consequently tune its structural transition and thermal expansion coefficient. Moreover, the size reduction effects on $LaFe_{11.9}Mn_{0.27}Si_{1.29}H_x$ morphological, microstructural, magnetic and thermal expansion properties were thoroughly characterized and correlated providing a comprehensive physical model for the observed behaviors.


2. Experimental Information

The $LaFe_{11.9}Mn_{0.27}Si_{1.29}H_x$ sample was prepared by arc-melting followed by hydrogenation [49]. After melting, to ensure homogeneity of the as-cast alloy, the ingot was encapsulated in quartz tubes under an Ar atmosphere and then annealed at 1050°C for 7 days and subsequently quenched in water. Hydrogenation was carried out on 1-2 mm fragments of the parent bulk sample in a furnace filled with 0.9 bar H_2 atmosphere, at 723 K for one hour, to saturate the H concentration. The as-prepared hydrogenated pieces of $LaFe_{11.9}Mn_{0.27}Si_{1.29}H_x$ alloy were hand-milled for a short period of time, resulting in an initial set of particles with a 100 µm average

size and a size distribution width (FWHM) of 126 μm (Figure 1 A). This sample is termed "as-prepared" throughout this manuscript. Roughly two grams of the as-prepared sample were placed inside a zirconia vessel together with four zirconia spheres of 5 mm radius and 38 g mass. No liquid media was included in the vessel. The ball to powder mass ratio was estimated to be 76. The vessel was installed in a FRITSCH PULVERISETTE 23 Mini Mill, and the powder was milled with a 50 Hz vertically oscillating frequency. Every 5 minutes, the milling was paused for 5 minutes to prevent any overheating of the vessel and the powder. The total milling time was 180 minutes, and at 15, 30, 45, 90 and 180 minutes, roughly 100 milligrams of the $LaFe_{11.9}Mn_{0.27}Si_{1.29}H_x$ milled powder were extracted and thoroughly characterized. These different powder samples have been termed respectively as BM15, BM30, BM45, BM90 and BM180. Every sample's chemical, micro, atomic structure, magnetic and thermal expansion properties were characterized as described below. All samples' morphology and chemical composition were investigated by scanning electron microscopy (SEM) and energy dispersive spectroscopy (EDS) using FEI Quanta 400FEG ESEM / EDAX Genesis X4M equipment. SEM image statistical analysis was performed using the ImageJ open source software [50]. Several hundreds of particles from the SEM images were randomly chosen for each sample to determine the particle size distribution, namely the average particle size and the size standard deviation. Magnetic characterizations of the powder samples were performed in a commercial Superconducting Quantum Interference Device (SQUID) magnetometer (MPMS3, by Quantum Design) by measuring their magnetization as a function of temperature between 350 K and 5 K while cooling with a magnetic field of 1000 Oe and by measuring isothermally their magnetization as a function of magnetic field at 20K. All magnetic measurements were measured under identical geometries and were properly corrected for inevitable deviations to the dipole approximation in accordance with the recent report by Amorim and co-authors [62]. The room-temperature crystal lattice parameters were obtained by Rietveld refinements against X-ray diffractograms measured in a Rigaku SmartLab using a Cu X-ray source (Kα1 = 1.5406 Å). The samples' thermal expansion was evaluated through Rietveld refinements of X-ray diffractograms obtained while varying the temperature between 250 K and 350 K at 1K/min under heating and cooling, with each diffractogram corresponding to a 1 K step. These measurements were performed with synchrotron radiation (λ = 0.1173 Å) at the Advanced Photon Source (APS) of the Argonne National Laboratory (beamline 11-ID-C). Each powder sample was wrapped in Cu thin-foil such that the diffraction pattern include reflections linked to the cubic Cu phase. As Cu thermal expansion is very well known [51], a conversion of any

given unit cell volume to temperature can be made, which results in Cu working as a local sample thermometer.

3. Results and Discussion

3.1 Morphology
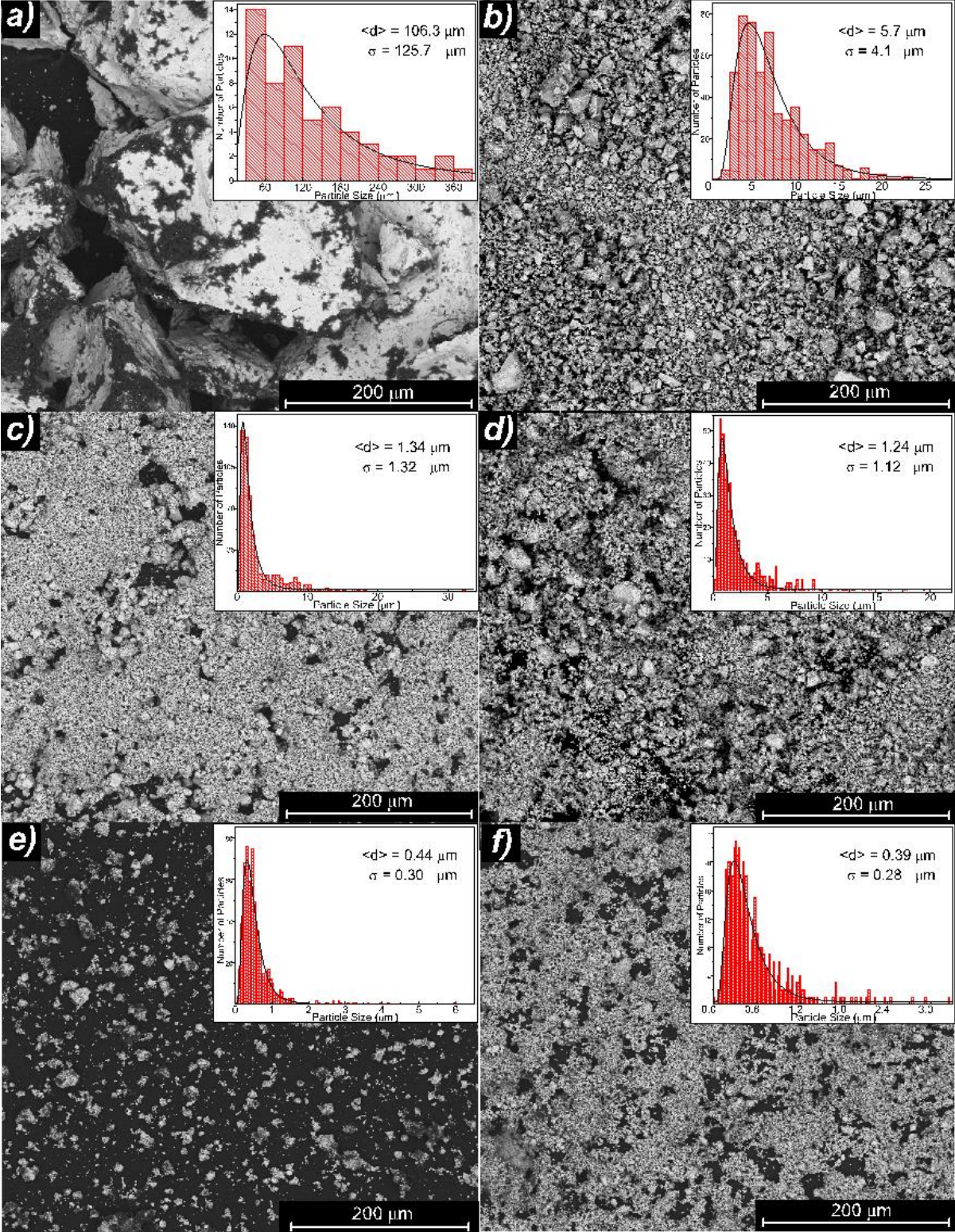
Figure 1. Scanning electron microscope (SEM) images obtained with backscattered electrons mode and size distribution histograms of $LaFe_{11.9}Mn_{0.27}Si_{1.29}H_x$ for the **a)** as-prepared, **b)** BM15, **c)** BM30, **d)** BM45, **e)** BM90 and **f)** BM180 LaFe11.9Mn0.27Si1.29Hx samples.

Figure 1 shows the SEM images of all the samples and their corresponding particle size distributions and lognormal fits. We have obtained a 96 % average particle size reduction from 106 μm for the as-prepared sample to 0.39 μm for the maximum BM time, t_{BM}, of 180 min, together with a 98 % reduction of the standard deviation.

3.1. Phase Composition and Crystal Structure
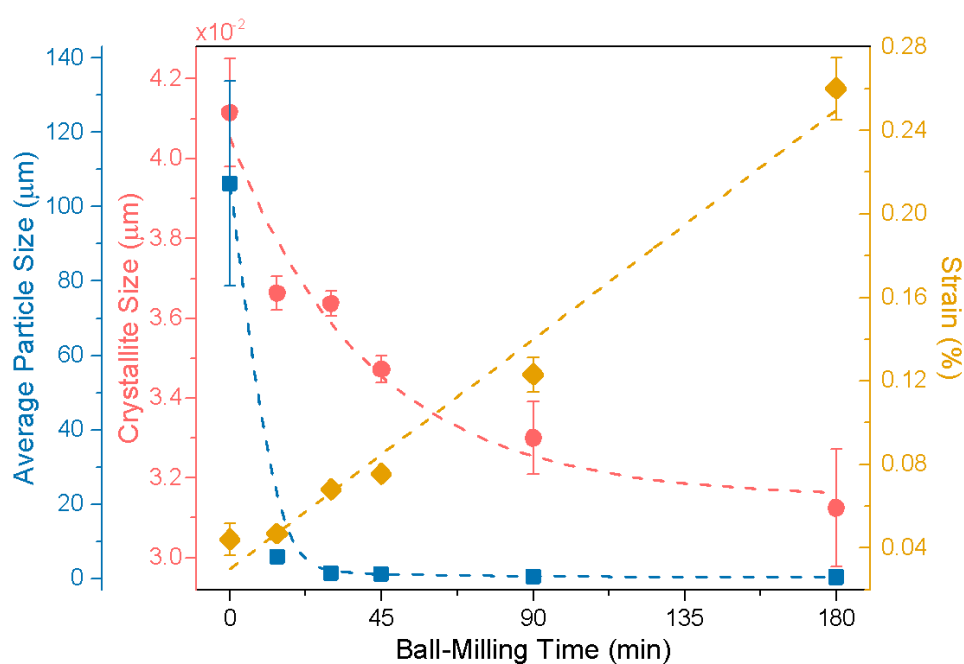
Figure 2: Average particle size (blue squares), crystallite size (red circles) and strain (yellow rhombus) of $LaFe_{11.9}Mn_{0.27}Si_{1.29}H_x$ samples as a function of ball-milling time. The error bars of the average particle size that are not visible are contained within the data squares area.

$LaFe_{11.9}Mn_{0.27}Si_{1.29}H_x$ has the NaZn13-type crystal structure (space group *Fm-3c*), where the Fe atoms, 8b (Fe(I)) and 96i (Fe(II)) occupy two nonequivalent 8b (Fe(I)) and 96i (Fe(II)) sites, and Si atoms occupy preferentially Fe(II) sites [11,35], Mn atoms tend to occupy equally both Fe(I) and Fe(II) sites [38,39] and the hydrogen atoms lie at interstitial sites [41] - see Figure S1 in Supplementary Information (S.I.). The Rietveld refinements against all X-Ray diffractograms at 273.6 K reveal the expected NaZn13-type crystal structure and a minority phase fraction of α-Fe (space group *Im-3m*), which is commonly observed in samples prepared

by this route [40]. An X-Ray diffractogram with a Rietveld Refinement of sample BM15 is presented in Figure S2 (S.I.). In addition, peaks due to the Cu cubic phase (space group *Fm-3m*) used for sample wrapping are identified and fitted.

Figure 2 displays the average particle size, crystallite size, and strain as a function of t_{BM}. The average particle size was obtained by SEM statistical image analysis. In contrast, the crystallite size (D) and strain (ε) were obtained through a linear regression following the Williamson-Hall relationship (see Figure S3 (S.I.)):

$$w \cos \theta = \frac{0.94\,\lambda}{D} + 4\,\varepsilon \sin \theta \qquad (1)$$

where w is the FWHM of the XRD peaks corresponding to the La(Fe$_{1-x}$,Si$_x$)$_{13}$ structure, λ is the incident X-ray wavelength, and θ is the peak position. [52-55]

Increasing t_{BM} leads to a decrease in average particle and crystallite sizes following a decreasing trend, Figure 2. Comparing the as-prepared and BM180 samples, the crystallite size decrease from 41.1 to 33.0 nm. Simultaneously, BM induces strain, which can be caused by the higher number of crystallites (and correspondingly a higher number of grain boundaries), high induced chemical disorder, grain surface relaxation and nonuniform lattice distortions [42,43,46,55]. Additionally, one can observe that both, particle size and crystallite size, display an inverse trend in comparison with the strain [55]. Strain increases linearly with t_{BM}, from 0.044 % (for the as-prepared sample) to 0.26 % (for the BM180 sample). A linear fit to this behaviour yields a 1.22×10^{-5} slope, meaning that a strain of ~ 1.22×10^{-3} % is induced per every minute of BM. So, by relative comparison, it is possible to conclude that BM time has a greater impact on the strain than on the crystallite size.

3.2. Magnetic Transition

Since the NTE behaviour of La(Fe$_{1-x}$,Si$_x$)$_{13}$-based compounds family is strongly correlated with its magnetic transition, magnetization versus temperature measurements were performed in all samples. Figure 3 a) shows the temperature dependence of the normalized magnetization ($M/M_{T=250K}$), $M(T)$, measured on cooling and with an applied magnetic field of 1 kOe, in the temperature range from 250 to 350 K for all samples. Figure 3 b) shows the derivative of the $M(T)$ curves, $dM/dT(T)$. From these curves, one can extract the Full Width at Half Maximum (FWHM = $\Delta T_{dM/dT}$), and the absolute value of their global minimum peaks, dM/dT_{peak}. Figure 3 c) shows the $\Delta T_{dM/dT}$ as a function of t_{BM} and also the slope of the $M(T)$ curves, slope $M/M_{T=250K}$, evaluated in the respective temperature range corresponding to $\Delta T_{dM/dT}$.
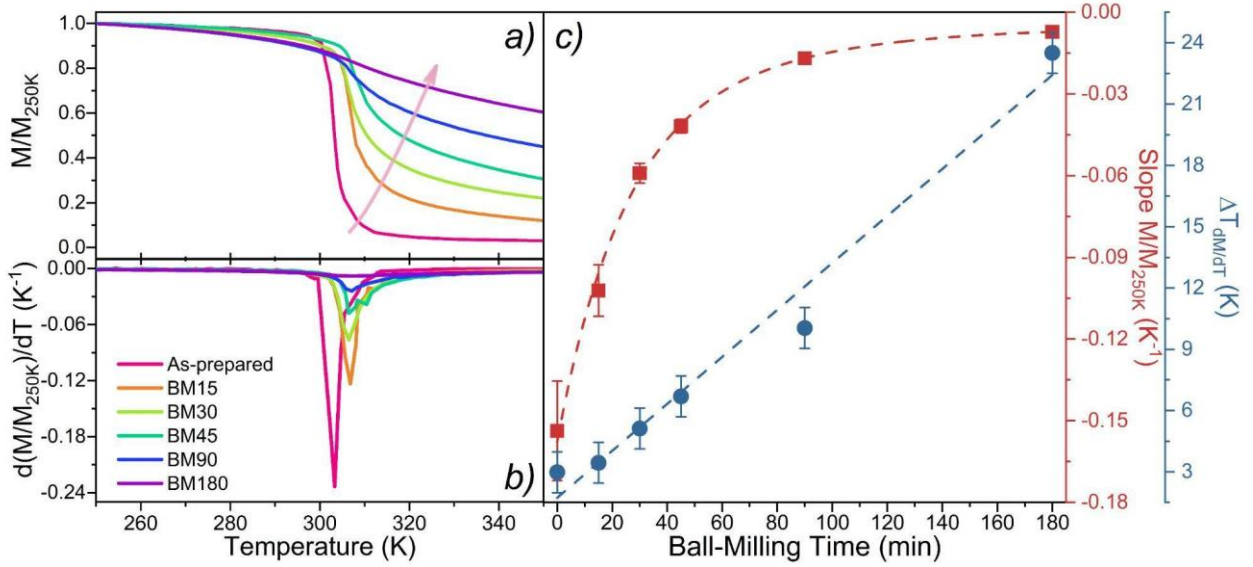
Figure 3. a) Normalized magnetization, $M/M_{T=250K}$, and **b)** dM/dT (T) of the as-prepared, BM15, BM30, BM45, BM90 and BM180 LaFe$_{11.9}$Mn$_{0.27}$Si$_{1.29}$H$_x$ samples, measured in cooling with an applied field of 1 KOe. **c)** Slope of the $M(T)$ curves within the FWHM of the dM/dT curve (red squares) and the corresponding temperature window width of the FWHM, $\Delta T_{dM/dT}$, (blue dots) as a function of ball-milling time.

The magnetization increases on cooling, revealing the typical PM-FM phase transition at T_C. The as-prepared sample presents a sharp transition at $T_C \sim 305$ K, and its magnetization then remains nearly constant with further temperature decrease. In comparison, the $M(T)$ profiles of the BM samples present an increasingly smoother transition with increasing t_{BM}. In fact, the $M/M_{T=250K}$ (T= 350 K) value increases monotonously as the t_{BM} increases, indicating that the FM-PM transition becomes more gradual with t_{BM}.

The dM/dT_{peak} quantifies the "abruptness" of the phase transition (also known as the thermomagnetic coefficient) and indicates the temperature at which the magnetization is changing most drastically, corresponding to $T \sim T_C$. Its dependence on t_{BM} is represented in Figure S4 (S.I.) where a reduction from ~ 0.23 K^{-1} (as-prepared) to ~ 0.01 K^{-1} (BM180) is observed.

The $\Delta T_{dM/dT}$ quantifies how broad the magnetic transitions are across temperature. This quantity varies approximately linearly with t_{BM} - increasing from ~ 3 K (as-prepared) to ~ 24 K (BM180), which shows how the broadening of the magnetic transition evolves with t_{BM}.

The slope of the $M(T)$ curves decrease rapidly with t_{BM} - decreasing from ~ 0.15 K^{-1} (as-prepared) to ~ 0.01 K^{-1} (BM180). This means that the temperature-induced magnetization variation is strongly suppressed as t_{BM} increases. In addition, the profile of the slope of the $M(T)$ curves versus t_{BM}, Figure 3 c), shows an exponential-like behaviour, as its values decay until a plateau region is reached - suggesting that increasing t_{BM} further will not promote significant slope changes.

3.2.1. Bean-Rodbell Analysis

From a theoretical point of view, the Bean-Rodbell model has been particularly successful in explaining and predicting the magnetic transitions of materials with strong magnetovolume coupling [56-59]. This model relies on the simple and observable assumption that the T_C of a strongly coupled magnetovolume material depends on the unit cell volume (hence strain) via a β coefficient (proportional to dT_C/dV). In addition, this model also introduced a new term η, which is dependent on β and on the material compressibility (K), allowing us to quantitatively distinguish materials with strong ($\eta > 1$) and weak ($\eta < 1$) magnetovolume coupling. The $M(T)$ curves were fitted (see Figure S5 in S.I) using the Bean-Rodbell model, assuming that the transition can be described not by a single T_C, but instead by a lognormal distribution of T_C's (associated with the induced microstrain), with a given width, ΔT_{T_C}, assuming fixed values for spin (0.92) and η (1.8) – in accordance with references [63, 64]. As can be seen in Figure S6 in S.I., ΔT_{T_C} increases drastically with t_{BM} from ~ 3 K (as-prepared) up to ~ 110 K (BM180). Similarly to the strain and the $\Delta T_{dM/dT}$, the ΔT_{T_C} displays a linear relationship with t_{BM}.

3.3. Thermal Expansion Characterization

Figure 4 a) shows the relative variation of the volume of the unit cell as a function of the temperature $\Delta V = (V(T) - V(T = 250\ K))/V$. Figure 4 b) shows the temperature derivative of the $\Delta V/V(T)$ curves, which is the equivalent to the coefficient of thermal expansion as a function of temperature, $\alpha_V(T)$. From this curve one obtains the FWHM, ΔT_{α_V}, and the value of its global minimum peak, $\alpha_V(T)_{peak}$. Figure 4 c) shows the value of the linear thermal expansion coeffient, $\underline{\alpha}_V$, evaluated in a temperature window defined by the ΔT_{α_V}, and the ΔT_{α_V} as a function of t_{BM}.
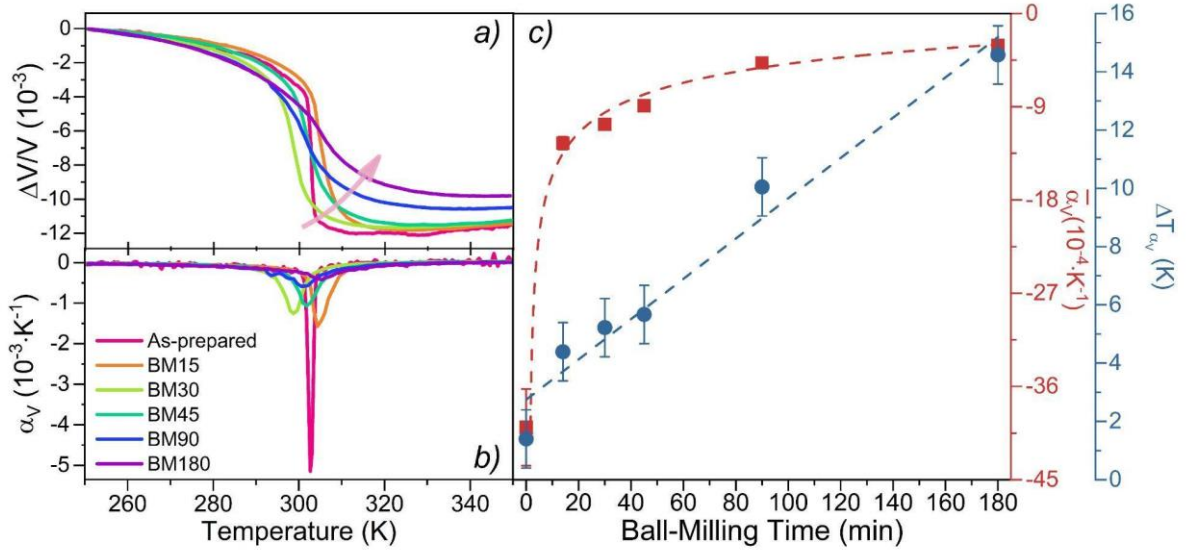
Figure 4. a) $\Delta V/V(T)$ and **b)** α_V of the as-prepared, BM15, BM30, BM45, BM90 and BM180 LaFe$_{11.9}$Mn$_{0.27}$Si$_{1.29}$H$_x$ samples, measured in cooling as a function of temperature. **c)** $\underline{\alpha}_V$ (red dots), evaluated in the ΔT_{α_V}; and the value of the ΔT_{α_V} (blue dots) as a function of the ball-milling time.

$\Delta V/V(T)$ curves show that the volume decreases with the increasing temperature, i.e. $\alpha_V < 0$ demonstrating NTE behaviour across the transition. In addition, the evolution of the $\Delta V/V(T)$ curves' profiles with t_{BM} is very similar to the evolution of the $M(T)$ curves' profiles: a gradual broadening of the transitions, as a result of the strong magnetovolume coupling. In addition, the overall $\Delta V/V$ variation tends to diminish with t_{BM}: the as-prepared sample has an overall $\Delta V/V$ of $\sim 11.5 \times 10^{-3}$, whereas the BM180 has $\sim 9.8 \times 10^{-3}$.

The $\alpha_V(T)_{peak}$ dependency with t_{BM} is shown in Figure S7 (S.I.), where a value of $\sim 2210 \times 10^{-6} \cdot K^{-1}$ is observed for the as-prepared sample, and a value of $\sim 260 \times 10^{-6} \cdot K^{-1}$ was obatined for the BM180 sample.

ΔT_{α_V} shows a linear trend with t_{BM} - increasing from ~ 1 K (as-prepared) to ~ 15 K (BM180). Similarly to what was observed with the magnetic transition, the $\underline{\alpha}_V$ decreases rapidly with t_{BM} - from $\sim 40 \times 10^{-4} \cdot K^{-1}$ (as-prepared) to $\sim 3 \times 10^{-4} \cdot K^{-1}$ (BM180). Additionally, the $\underline{\alpha}_V$ tends to decrease rapidly with t_{BM}, reaching then a plateau region. As occurred with the magnetization slope, this behaviour suggests that further BM will not induce significant $\underline{\alpha}_V$ values changes in the temperature range defined. Hence, the $\underline{\alpha}_V$ and the ΔT_{α_V} behaviours clearly demonstrate that

t_{BM} is linearly expanding the temperature interval where the transition occurs and, concomitantly, turning it less sharp.

The $\alpha_V(T)$ was also analyzed in the whole temperature interval, from 250 to 350 K, $\underline{\alpha}_{V\,[250-350\,K]}$. Figure S8 (S.I.) shows the relation between the $\underline{\alpha}_{V\,[250-350\,K]}$ and t_{BM}, where a linear relation is observed. The as-prepared sample shows a $\underline{\alpha}_{V\,[250-350\,K]}$ of ~ -115×10^{-6}·K^{-1} and the BM180 a $\underline{\alpha}_{V\,[250-350\,K]}$ of ~ -98×10^{-6}·K^{-1}.

Figure 5 shows the relation between the crystallite size and strain with the linear $\underline{\alpha}_{V\,[250-350\,K]}$. Since the $\underline{\alpha}_{V\,[250-350\,K]}$ is proportional to the t_{BM}, the relation between the $\underline{\alpha}_{V\,[250-350\,K]}$ and the crystallite size and strain is similar to the relation between these two variables and t_{BM}, as shown in Figure 2.

In order to try to disentangle the roles of crystallite size and induced microstrain on the observed changes of the magnetic and structural transitions with milling time, the raw patterns, the unit cell volume, the Fe^{I}-Fe^{II} interatomic distances (known to be the interatomic distance influencing Tc the most and the Tc [15, 37, 60]) and the Tc were plotted against ball milling time as can be seen in Figures S13, S14 and S15 in the supplementary information file. The absence of significant or monotonous changes observed in the center peaks position, unit cell volume, Fe^{I}-Fe^{II} interatomic distances or Tc as a function of milling time, coupled with the clear, symmetric and linear broadening of the diffraction and magnetization derivative peaks, strongly suggests that the linearly increasing microstrain has the main role on tuning the magnetic and structural transitions. This physical picture is further corroborated by the Bean-Rodbell analysis where a linearly increasing broadening of the Tc distribution is required to fit the measured M(T) curves as a function of milling time (Figure S6)."

Additionally, in order to further untangle the effect of size-confinement from that of induced microstrain, we have measured low-temperature (20K), isothermal magnetization versus magnetic field curves for the as-prepared and BM180 samples, as plotted in Figure S12. As can be seen, the saturation magnetization remains nearly unchanged after the total 180 minutes of milling. This behavior contrasts with the behavior found for La-Fe-Si nanoparticles, where a 30% decrease on the saturation magnetization was observed [61]. In fact, the suppression of the magnetization values together with shift of the transition temperatures, are typically observed in a wide range of nanostructured magnetocaloric materials [47]. Hence, these results demonstrate that the milling is not changing the individual magnetic moments, but instead is inducing magnetic disorder (due to the structural disorder - microstrain) which manifests itself in broadened magnetic and structural phase transitions.
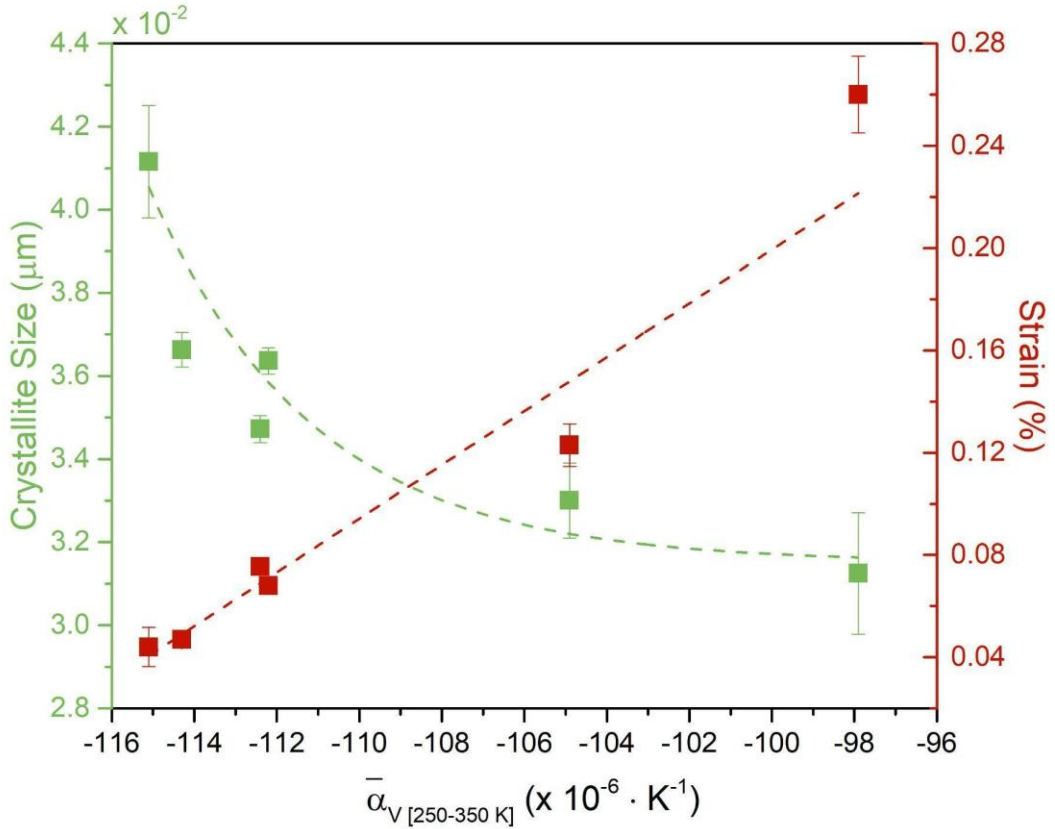
Figure 5. Crystallite size (green squares) and strain (red circles) dependence with the $\underline{\alpha}_{V\,[250-350\,K]}$ of all the samples.

Interestingly, comparing the magnetic and structural transitions as seen in Figure S10, we can see that the relative variation in magnetization between 250 K and 350 K is more pronounced than the relative change in unit cell volume. This suggests that the magnetic correlations are more sensitive to strain than the unit cell volume of the sample.

Figure 6 a) and b) displays the contour plots (colour-maps) of the strain and crystallite size as a function of the slope parameters $\underline{\alpha}_V$ and $M/M_{T=250K}$ slope, respectively. We used (crystallite size, strain, $\underline{\alpha}_V$) and (crystallite size, strain, $M/M_{T=250K}$ Slope) experimental data for each sample (both of which are specified in table 1) to perform a numerical estimation of 100 new data points by a method for interpolating spatial data. Gridding methods to convert XYZ data into a matrix were performed using the Kriging method algorithm.

Using this interpolation method, we are able to create an estimation for new values of $\underline{\alpha}_V$ and $M/M_{T=250K}$ slope for a range of strain and crystallite size values. The obtained (strain, crystallite size, $\underline{\alpha}_V$) and (strain, crystallite size, $M/M_{T=250K}$ Slope) matrices were then plotted

in 3D contour plots represented in Figures 6 a) and b), respectively. One can observe that higher values of $\underline{\alpha}_V$ coincide with higher values of crystallite size and lower values of strain, corresponding to samples that were not milled. As one decreases the crystallite size and continuously increases the strain, the $\underline{\alpha}_V$ decreases drastically (nearly by two orders of magnitude). This further highlights the role of the strain and crystallite size on ruling the $\alpha_V(T)$ of these materials while providing pathways for further thermal expansion coeffient tailoring. A remarkably similar colour pattern is observed in Figure 6 b), which underlines the resemblance of the magnetic and structural transitions and how they evolve similarly with controllable strain and crystallite sizes.
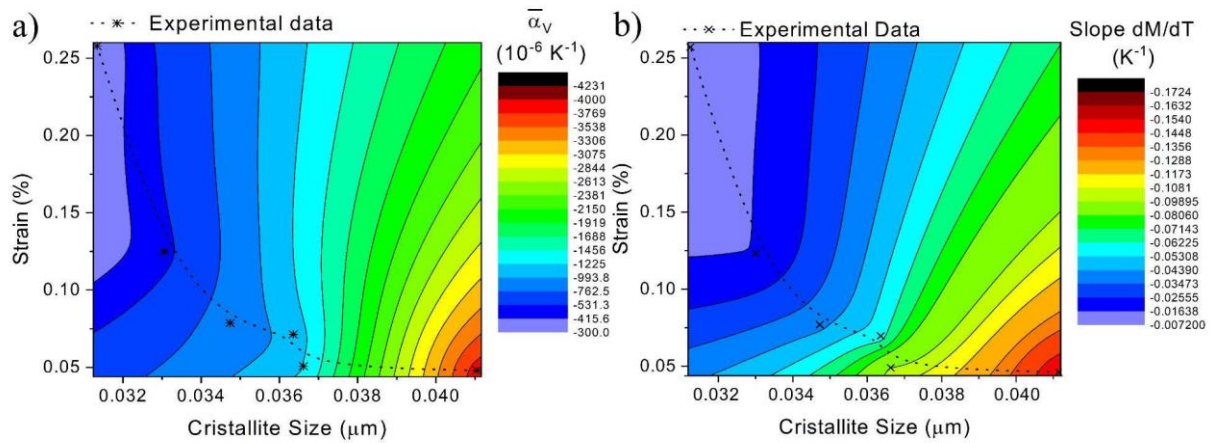
Figure 6. a) Contour plot of the $\underline{\alpha}_V$ colour code (where red and blue represent larger and smaller absolute values, respectively) evaluated at the ΔT_{α_V} temperature window as a function of strain and crystallite size. b) Contour plot of the $M(T)$ slope colour code (where red and blue represent larger and smaller absolute values, respectively) evaluated at the $\Delta T_{dM/dT}$ temperature window as a function of strain and crystallite size. Both contour plots were performed by interpolation of the experimental values.

Table 1 summarizes the most relevant parameters evaluated throughout this work.

Ball-Milling time	Strain	Crystallite Size	$\underline{\alpha}_{V\,[250-350\,K]}$	T_C	ΔT_{T_C}	ΔT_{α_V}	$\Delta T_{dM/dT}$	$\underline{\alpha}_V$	$M/M_{T=250K}$ Slope	Average Particle Size
(min)	(%)	(μm)	($\times 10^{-6}\cdot K^{-1}$)	(K)	(K)	(K)	(K)	($\times 10^{-6}\cdot K^{-1}$)	(K^{-1})	(μm)
0	0.044	0.0412	-115.1	304	3	1.40	2.98	-3994.18	-0.154	106.30
15	0.047	0.0366	-114.3	307	6.5	4.39	3.44	-1251.41	-0.102	5.74
30	0.068	0.0364	-112.2	307	12	5.22	5.12	-1069.88	-0.059	1.35
45	0.076	0.0347	-112.4	306	15	5.67	6.69	-890.71	-0.042	1.24
90	0.123	0.0330	-104.9	307	33	10.05	10.04	-476.45	-0.017	0.44
180	0.260	0.0313	-97.9	307	110	14.58	23.51	-307.74	-0.007	0.39

Table 1. Most relevant values used throughout the work: ball-milling time (t_{BM} (min)); strain (%); crystallite size (μm); linear coefficient of thermal expansion ($\underline{\alpha}_{V\,[250-350\,K]}$ ($\times 10^{-6}\cdot K^{-1}$)) evaluated in the temperature range of 250 to 350 K; curie temperature (T_c) (K); full width at half maximum (FWHM) of the T_c distribution (ΔT_{T_C} (K)); FWHM of the α_V curve (ΔT_{α_V} (K)); FWHM of the dM/dT curve ($\Delta T_{dM/dT}$ (K)); linear coefficient of thermal expansion evaluated in the ΔT_{α_V} ($\underline{\alpha}_V$ ($\times 10^{-6}\cdot K^{-1}$)); slope of the $M(T)$ curve evaluated at the $\Delta T_{dM/dT}$ ($M/M_{T=250K}$ slope (K^{-1})); average particle size (μm).

4. Conclusion

In summary, BM leads to a significant reduction of the average particle and crystallite size and to a drastic linear enhancement of the induced microstrain in LaFe$_{11.9}$Mn$_{0.27}$Si$_{1.29}$H$_x$. A severe broadening of the magnetization versus temperature profiles across T_C is observed, quantified by a 93% suppression of its $M/M_{T=250K}$ slope and a 88% enhancement of the transition width ($\Delta T_{dM/dT}$). In the framework of the Bean-Rodbell model, such transition widening can be explained by the presence of an-ever wider T_C distribution as a consequence of the increased induced microstrain (via t_{BM}). Due to strong magnetovolume coupling, both unit cell volume and magnetization dependence on temperature show a remarkably similar evolution with BM time. In particular, the $\alpha_V\,(T)_{peak}$ decreases from ~ 2210 (as-prepared) down to ~ 260 ppm·K^{-1} (after 180 minutes of BM), and the averaged α_V in the temperature range from 250 to 350 K, $\underline{\alpha}_{V\,[250-350\,K]}$, decreases from -115$\times 10^{-6}\cdot K^{-1}$ (as-prepared) to -98$\times 10^{-6}\cdot K^{-1}$ (BM180).

This work demonstrates that the crystallite size and the ball-milled induced microstrain (in particular the latter) are remarkably efficient tools to tune and customize the thermal expansion coefficient of La(Fe$_{1-x}$,Si$_x$)$_{13}$-based compounds. Combining the method presented here with the usual chemical control method, a synergistic effect is expected towards the development of a near-zero thermal expansion material. In addition, this La(Fe$_{1-x}$,Si$_x$)$_{13}$ size-control study triggers an opening research window for other negative thermal expansion materials with strong magnetovolume coupling.

Finally, by inducing strain through a process like ball-milling, one is actively reducing the materials' particle size, which demonstrates favorability for technological applications, since for the same filler content (%), smaller NTE particles are more effective in tuning (decreasing) a composite thermal expansion than larger ones [65-68] enabling a controllable and homogenous compensating mechanism.

6. Supporting Information

The supporting information file contains the following contents:

- Schematic picture of $LaFe_{11.9}Mn_{0.27}Si_{1.29}H_x$ crystal structure (Figure S1);

- X-ray diffractogram of $LaFe_{11.9}Mn_{0.27}Si_{1.29}H_x$ at 273K and the corresponding Rietveld refinement (Figure S2);

- Williamson-Hall analysis plot for the estimation of crystallite size (D) and strain (ε) (Figure S3) ;

- Evolution of the magnetization temperature derivative peak value as function of ball milling time (Figure S4);

- As prepared sample normalized magnetization versus temperature curve and the respective fit within the Bean-Rodbell model with a Tc distribution (Figure S5);

- Evolution of Tc full width at half maximum (FWHM) distribution and strain (%) with ball milling time (Figure S6);

- Peak value of thermal expansion coefficient as a function of ball milling time (Figure S7);

- Averaged (in the 250-350K) thermal expansion coefficient as a function of ball milling time (Figure S8);

- Unit cell volume change and respective temperature derivatives, and normalized magnetization and respective temperature derivatives for as-prepared and ball milled samples for 45 and 180 minutes (Figure S9);

- Relative change of unit cell volume and magnetization between 250 and 350K temperatures (Figure S10);

- Unit cell volume change and respective temperature derivative, and normalized magnetization and respective temperature derivative for as-prepared sample plotted together with linear fittings within the FWHM temperature range (Figure S11);

- Magnetization versus magnetic field curves measured at 20K of the as-prepared and ball-milled for 180 minutes samples (Figure S12);

- Raw XRD patterns for the as-prepared and ball-milled for 180 minutes samples (Figure S13);

- Evolution of the unit cell volume and Fe^I-Fe^{II} interatomic distances at 250K and 350K as a function of ball milling time (Figure S14);

- Averaged Curie temperature and full width at half maximum of the magnetization derivative peak as a function of ball milling time (Figure S15);

6. References

[1]   Barrera, G. D.; Bruno, J. A. O.; Barron, T. H. K.; Allan, N. L. Negative Thermal Expansion. *Journal of Physics Condensed Matter*. **2005**, *17* (4)*.* DOI: 10.1088/0953-8984/17/4/R03.

[2]   Miller, W.; Smith, C. W.; Mackenzie, D. S.; Evans, K. E. Negative Thermal Expansion: A Review. *Journal of Materials Science*. **2009**, *44* (20)*,* 5441-5451. DOI: 10.1007/s10853-009-3692-4.

[3]   Attfield, J. P. Mechanisms and Materials for NTE. *Frontiers in Chemistry.* **2018**, *6*. DOI: 10.3389/fchem.2018.00371.

[4]   Takenaka, K. Progress of Research in Negative Thermal Expansion Materials: Paradigm Shift in the Control of Thermal Expansion. *Frontiers in Chemistry.* **2018**, *6*. DOI: 10.3389/fchem.2018.00267.

[5]   Song, Y.; Shi, N.; Deng, S.; Xing, X.; Chen, J. Negative thermal expansion in magnetic materials. *Progress in Materials Science*. **2021**, *121*. DOI: 10.1016/j.pmatsci.2021.100835.

[6]   Chen, J.; Hu, L.; Deng, J.; Xing, X. Negative Thermal Expansion in Functional Materials: Controllable Thermal Expansion by Chemical Modifications. *Chemical Society reviews*. **2015**, *44,* 3522-3567. DOI: 10.1039/c4cs00461b.

[7]   Liang, E.; Sun, Q.; Yuan, H.; Wang, J.; Zeng, G.; Gao, Q. Negative thermal expansion: Mechanisms and materials. *Frontiers of Physics*. **2021**, *16, 53302*. DOI: 10.1007/s11467-021-1070-0.

[8]   Zhang, Y.; Chen, B.; Guan, D.; Xu, M.; Ran, R.; Ni, M.; Zhou, W.; O'Hayre, R.; Shao, Z. Thermal-expansion offset for high-performance fuel cell cathodes. *Nature*. **2021**, *591*, 246-251. DOI: 10.1038/s41586-021-03264-1.

[9]   Li, S.; Huang, R.; Zhao, Y.; Wang, W.; Han, Y.; Li, L. Zero Thermal Expansion Achieved by an Electrolytic Hydriding Method in La(Fe,Si)13 Compounds. Advanced Functional Materials. **2016**, *27* (5). DOI: 10.1002/adfm.201604195.

[10]   Wang, W.; Huang, R.; Li, W.; Tan, J.; Zhao, Y.; Li, S.; Huang, C.; Li, L. Zero thermal expansion in NaZn13-type La(Fe,Si)13 compounds. *Physical Chemistry Chemical Physics.* **2015**, *17*, 2352-2356. DOI: 10.1039/C4CP04672B.

[11]   Auckett, J. E.; Barkhordarian, A. A.; Ogilvie, S. H.; Duyker, S.; Chevreau, H.; Peterson, V. K.; Kepert, C. J. Continuous negative-to-positive tuning of thermal expansion achieved by controlled gas sorption in porous coordination frameworks. *Nature Communications.* **2018**, *9*, 4873. DOI: 10.1038/s41467-018-06850-6.

[12]   Lin, J. C.; Tong, P.; Zhou, X. J.; Lin, H.; Ding, Y. W.; Bai, Y. X.; Chen, L.; Guo, X. G.; Yang, C.; Song, B.; Wu, Y.; Lin, S.; Song, W. H.; Sun, Y. P. Giant negative thermal expansion covering room temperature in nanocrystalline GaNxMn3. *Applied Physics Letters.* **2015**, *107*, 131902. DOI: 10.1063/1.4932067.

[13]   Li, Q; Zhu, H.; Hu, L.; Chen, J.; Xing, X. Negative Thermal Expansion in Nanosolids. *Accounts of Chemical Research.* **2019**, *52* (9), 2694-2702. DOI: 10.1021/acs.accounts.9b00260.

[14]   Liu, J.; Gong, Y.; Wang, J.; Peng, G.; Miao, X.; Xu, G.; Xu, F. Realization of zero thermal expansion in La(Fe,Si) 13-based system with high mechanical stability. *Materials and Design.* **2018**, *148*, 71-77. DOI: 10.1016/j.matdes.2018.03.057.

[15]   Huang, R.; Liu, Y.; Fan, W.; Tan, J.; Xiao, F.; Qian, L.; Li, L. Giant Negative Thermal Expansion in NaZn13-Type La(Fe, Si, Co)13 Compounds. *J Am Chem Soc.* **2013**, *135* (31), 11469-11472. DOI: 10.1021/ja405161z.

[16]   Belo, J. H.; Pires, A.; Gomes, I.; Andrade, V.; Sousa, J.; Hadimani, R.; Jiles, D.; Ren, Y.; Zhang, X.; Araujo, J.; Pereira, A. Giant negative thermal expansion at the nanoscale in the multifunctional material Gd5(Si,Ge)4. *Physical Review B.* **2019**, *100*. DOI: 10.1103/PhysRevB.100.134303.

[17]   Jia, L.; Sun, J. R.; Zhang, H. W.; Hu, F. X.; Dong, C.; Shen, B. G. Magnetovolume effect in intermetallics LaFe13−xSix. *Journal of Physics Condensed Matter.* **2006**, *18*, 9999. DOI: 10.1088/0953-8984/18/44/002.

[18]   Sun, W.; Zhang, H.; Li, W.; Huang, R.; Zhao, Y.; Wang, W.; Li, L. Controllable negative thermal expansion in NaZn13-type La(Fe, Co, Al)13 compounds. *AIP Advances.* **2020**, *10*, 075123. DOI: 10.1063/5.0010204.

[19]   Li, W-H.; Wu, S. Y.; Yang, C. C.; Lai, A. S. K. L.; Lee, K. C.; Huang, H. L.; Yang, H. D. Thermal Contraction of Au Nanoparticles. *Phys. Rev. Lett..* **2022**, *89* (13): 135504. DOI: 10.1103/PhysRevLett.89.135504.

[20]   Hao, Y.; Zhang, X.; Wang, B.; Yuang, Y.; Wang, F. Anomalous thermal expansion and magnetic properties of Tm2Fe17−xCrx compounds. *Journal of Applied Physics.* **2010**, *108*, 023915. DOI: 10.1063/1.3456444.

[21]   Sumiyama, K.; Shiga, M.; Morioka, M.; Nakamura, Y. Characteristic magnetovolume effects in Invar type Fe-Pt alloys. *Journal of Physics F: Metal Physics.* **1979**, *9* (8), 1665–1677. DOI: 10.1088/0305-4608/9/8/017.

[22]   Mary, T. A.; Evans, J. S. O.; Vogt, T.; Sleight, A. W. Negative Thermal Expansion from 0.3 to 1050 Kelvin in ZrW2O8. Science. **1996**, *272*, 90-92. DOI: 10.1126/science.272.5258.90.

[23]   Yu, C.; Lin, K.; Jiang, S.; Cao, Y.; Li, W.; Wang, Y.; Chen, Y.; An, K.; You, L.; Kato,

K.; Li, Q.; Chen, J.; Deng, J.; Xing, X. Plastic and low-cost axial zero thermal expansion alloy by a natural dual-phase composite. *Nature Communications*. **2021**, *12* (1): 4701. DOI: 10.1038/s41467-021-25036-1.

[24]   Takenaka, K.; Okamoto, Y.; Shinoda, T.; Katayama, N.; Sakai, Y. Colossal negative thermal expansion in reduced layered ruthenate. *Nature Communications*. **2017**, *8*, 14102. DOI: 10.1038/ncomms14102.

[25]   Mullaney, B. R.; Goux-Capes, L.; Price, D. J.; Chastanet, G.; Létard, J-F.; Kepert, C. J. Spin crossover-induced colossal positive and negative thermal expansion in a nanoporous coordination framework material. *Nature Communications*. **2017**, *8*, 1053. DOI: 10.1038/s41467-017-00776-1.

[26]   Yao, Z-S.; Guan, H.; Shiota, Y.; He, C-T.; Wang, X-L.; Wu, S-Q.; Zheng, X.; Su, S-Q.; Yoshizawa, K.; Kong, X.; Sato, O.; Tao, J. Giant anisotropic thermal expansion actuated by thermodynamically assisted reorientation of imidazoliums in a single crystal. *Nature Communications*. **2019**, *10*, 4805. DOI: 10.1038/s41467-019-12833-y.

[27]   Guo, X.; Ni, X. ; Li, J. ; Zhang, H.; Zhang, F.; Yu, H.; Wu, J.; Bai, Y.; Lei, H.; Huang, Y.; Rogers, J. A.; Zhang, Y. Designing Mechanical Metamaterials with Kirigami- Inspired, Hierarchical Constructions for Giant Positive and Negative Thermal Expansion. *Advanced Materials*. **2021**, *33*. DOI:10.1002/adma.202004919.

[28]   Xu, X.; Zhang, Q.; Hao, M.; Hu, Y.; Lin, Z.; Peng, L.; Wang, T.; Ren, X.; Wang, C. ; Zhao, Z.; Wan, C.; Fei, H.; Wang, L.; Zhu, J.; Sun, H.; Chen, W.; Du, T.; Deng, B.; Cheng, G.; Duan, X. Double-negative-index ceramic aerogels for thermal superinsulation. *Science*. **2019**, *363*, 723-727. DOI: 10.1126/science.aav7304.

[29]   Callen, E.; Callen H. B. Forced Magnetostriction, and Anomalous Thermal Expansion in Ferromagnets. *Phys. Rev.* **1965**, *139*, A455–A471. DOI: 10.1103/PhysRev.139.A455.

[30]   Shimizu, M. Itinerant electron magnetism. *Reports Prog. Phys.* **1981**, *44*, 329–409. DOI: 10.1088/0034-4885/44/4/001.

[31]   Andrade, V. M.; Amirov, A.; Yusupov, D.; Pimentel, B.; Barroca, N.; Pires, A. L.; Belo, J. H.; Pereira, A. M.; Valente, M. A.; Araujo, J. P.; Reis, M. S. Multicaloric effect in a multiferroic composite of Gd5(Si,Ge)4 microparticles embedded into a ferroelectric PVDF matrix. *Scientific Reports.* **2019**, *9*, 18308. DOI: 10.1038/s41598-019-54635-8.

[32]   Pereira, A. M.; Kampert, E.; Moreira, J. M.; Zeitler, U. ; Belo, J. H.; Magén, C.; Algarabel, P. A.; Morellón, L.; Ibarra, M. R.; Gonçalves, J. N.; Amaral, J. S. ; Amaral, V. S.; Sousa, J. B.; Araujo, J. P. Unveiling the (De)coupling of magnetostructural transition nature in magnetocaloric R5Si2Ge2 (R = Tb, Gd) materials. *Applied Physics Letters*. **2011**, *99*, 132510.

DOI: 10.1063/1.3640213.

[33]   Zheng, X. G.; Kubozono, H.; Yamada, H.; Kato, K.; Ishiwata, Y.; Xu, Ch. N. Giant Negative Thermal Expansion in Magnetic Nanocrystals. *Nature nanotechnology.* **2009**, *3*, 724-726. DOI: 10.1038/nnano.2008.309.

[34]   Paul-Boncour, V.; Bessais, L. Tuning the Magnetocaloric Properties of the La(Fe,Si)13 Compounds by Chemical Substitution and Light Element Insertion. *Magnetochemistry.* **2021**, *7* (1). DOI: 10.3390/magnetochemistry7010013.

[35]   Wang, W.; Huang, R.; Shan, Y.; Zhao, Y.; Shan, X.; Guo, S.; Huang, C.; Li, L. Adjustable thermal expansion in La(Fe, Si)13-based conductive composites by high-pressure synthesis. *Progress in Natural Science: Materials International.* **2019**, *29*, 28. DOI: 10.1016/j.pnsc.2019.01.008.

[36]   Wang, J.; Yuan-yuan, G.; Liu, J.; Miao, X.; Xu, G.; Chen, F.; Zhang, Q.; Xu, F. Balancing negative and positive thermal expansion effect in dual-phase La(Fe,Si) 13 /α-Fe in-situ composite with improved compressive strength. *Journal of Alloys and Compounds.* **2018**, *769*, 233. DOI: 10.1016/j.jallcom.2018.07.349.

[37]   Li, S.; Huang, R.; Zhao, Y.; Li, W.; Wang, W.; Huang, C.; Gong, P.; Lin, Z.; Li, L. Broad Negative Thermal Expansion Operation-Temperature Window Achieved by Adjusting Fe–Fe Magnetic Exchange Coupling in La(Fe,Si)13 Compounds. *Inorganic Chemistry.* **2015**, *54* (16), 7868-7872. DOI: 10.1021/acs.inorgchem.5b00908.

[38]   Li, W.; Huang, R.; Wang, W.; Liu, H.; Han, Y.; Huang, C.; Li, L. Low-temperature negative thermal expansion property of Mn doped La(Fe,Si)13 compounds. *Journal of Alloys and Compounds.* **2015**, *628*, 308. DOI: 10.1016/j.jallcom.2014.11.120.

[39]   Zhao, Y.; Huang, R.; Shan, Y.; Wang, W.; Li, J.; Li, L. Low-temperature abnormal thermal expansion property of Mn doped cubic NaZn13-type La(Fe, Al)13 compounds. *Journal of Physics: Conference Series.* **2017**, *897*. DOI: 10.1088/1742-6596/897/1/012005.

[40]   Krautz, M.; Skokov, K.; Gottschall, T.; Teixeira, C. S.; Waske, A.; Liu, J.; Schultz, L.; Gutfleisch O. Systematic investigation of Mn substituted La(Fe,Si)13 alloys and their hydrides for room-temperature magnetocaloric application. *Journal of Alloys and Compounds.* **2014**, *598*, 27-32. DOI: 10.1016/j.jallcom.2014.02.015.

[41]   Baumfeld, O. L.; Gercsi, Z.; Krautz, M.; Gutfleisch, O.; Sandeman, K. G. The dynamics of spontaneous hydrogen segregation in LaFe13−xSixHy. *Journal of Applied Physics.* **2014**, *115*, 203905. DOI: 10.1063/1.4879099.

[42]   Gottschall, T.; Benke, D.; Fries, M,; Taubel, A,; Radulov, I. A.; Skokov, K. P.; Gutfleisch, O. A Matter of Size and Stress: Understanding the First-Order Transition in

Materials for Solid-State Refrigeration. *Advanced Functional Materials*. **2017**, *27* (32). DOI: 10.1002/adfm.201606735.

[43]   Waske, A.; Giebeler, L.; Weise, B.; Funk, A.; Hinterstein, M.; Herklotz, M.; Skokov, K.; Fähler, S.; Gutfleisch, O.; Eckert, J. Asymmetric first-order transition and interlocked particle state in magnetocaloric La(Fe,Si)13. *physica status solidi (RRL) – Rapid Research Letters*. **2015**, *9* (2), 136-140. DOI: 10.1002/pssr.201409484.

[44]   Zavareh, M. G.; Skourski, Y.; Skokov, K. P.; Karpenkov, D. Y.; Zvyagina, L.; Waske, A.; Haskel, D.; Zhernenkov, M.; Wosnitza, J.; Gutfleisch, O. Direct Measurement of the Magnetocaloric Effect in La (Fe ,Si, Co)13 Compounds in Pulsed Magnetic Fields. *Physical Review Applied*. **2017**, *8*, 014037. DOI: 10.1103/PhysRevApplied.8.014037.

[45]   Karpenkov, D. Y.; Karpenkov, A. Y.; Skokov, K. P.; Radulov, I. A.; Zhelezdnyi, M.; Faske, T.; Gutfleisch, O.. Pressure Dependence of Magnetic Properties in La (Fe ,Si)13 : Multistimulus Responsiveness of Caloric Effects by Modeling and Experiment. *Physical Review Applied*. **2020**, *13*, 034014. DOI: 10.1103/PhysRevApplied.13.034014.

[46]   Brechtl, J.; Koehler, M. R.; Kesler, M. S.; Henderson, H. B.; Baker, A. A.; Li, K; Kiggans, J.; Nawaz, K.; Rios, O.; Momen, A.M. Effect of Composition on the Phase Structure and Magnetic Properties of Ball-Milled LaFe11.71-xMnxSi1.29H1.6 Magnetocaloric Powders. *Magnetochemistry*. **2021**, *7* (9)*, 132*. DOI: 10.3390/magnetochemistry7090132.

[47]   Belo, J. H.; Pires, A. L. ; Araújo, J. P. ; Pereira, A. M. Magnetocaloric materials: From micro- to nanoscale. *Journal of Materials Research*. **2018**, *1-24*, 134-157. DOI: 10.1557/jmr.2018.352.

[48]   Pires, A. L.; Belo, J. H.; Turcaud, J.; Oliveira, G. N. P.; Araujo, J. P.; Berenov, A.; Cohen, L. F.; Lopes, A. M. L.; Pereira, A. M. Influence of short time milling in R5(Si,Ge)4, R = Gd and Tb, magnetocaloric materials. *Materials & design*. **2015**, *85*, 32-38. DOI: 10.1016/j.matdes.2015.06.099.

[49]   Radulov, I. A.; Skokov, K. P.; Karpenkov, D. Y.; Gottschall, T.; Gutfleisch, O. On the preparation of La(Fe,Mn,Si)13H polymer-composites with optimized magnetocaloric properties. *Journal of Magnetism and Magnetic Materials*. **2015**, *396*. DOI: 10.1016/j.jmmm.2015.08.044.

[50]   ImageJ software, W.S. Rasband, ImageJ, U. S. National Institutes of Health, Bethesda, Maryland, USA, http://imagej.nih.gov/ij/, 1997-2012.

[51]   Wang, K.; Reeber, R. Thermal Expansion of Copper. *High Temperature and Materials Science*. **1996**, *35*, 181-186.

[52]   Zak, Ali K.; Majid, W. H Abd; Abrishami, M. E.; Yousefi, R. X-ray analysis of ZnO

nanoparticles by Williamson–Hall and size–strain plot methods. *Solid State Sciences.* **2011**, *13*, 251-256. DOI: 10.1016/j.solidstatesciences.2010.11.024.

[53]   Williamson, G. K.; Hall, W. H. X-ray line broadening from filed aluminium and wolfram. *Acta Metall.* **1953**, *1*. DOI: 10.1016/0001-6160(53)90006-6.

[54]   Proenca, M. P.; Sousa, C. T.; Pereira, A. M.; Tavares, P. B.; Ventura, J.; Vazquez, M.; Araujo, J. P. Size and surface effects on the magnetic properties of NiO nanoparticles. *Physical Chemistry Chemical Physics.* **2011**, *13*, 9561-9567. DOI: 10.1039/C1CP00036E.

[55]   Apolinário, A.; Lopes, T.; Costa, C.; Araujo, J. P.; Mendes, A. M. Multilayered WO3 Nanoplatelets for Efficient Photoelectrochemical Water Splitting: The Role of the Annealing Ramp. *ACS Applied Energy Materials.* **2019**, *2*, 1040-1050. DOI: 10.1021/acsaem.8b01530.

[56]   Amaral, J. S.; Amaral, V. S. Disorder effects in giant magnetocaloric materials. *Physica Status Solidi (A) Applications and Materials Science.* **2014**, *211*, 971-974. DOI: 10.1002/pssa.201300749.

[57]   Bean, C. P.; Rodbell, D. S. Magnetic Disorder as a First-Order Phase Transformation. *Physical Review - PHYS REV X.* **1962**, *126*, 104. DOI: 10.1103/PhysRev.126.104.

[58]   Belo, J. H.; Amaral, J. S. ; Pereira, A. M. ; Amaral, V. S. ; Araujo, J. P. On the Curie temperature dependency of the magnetocaloric effect. *Applied Physics Letters*. **2012**, *100* (24). DOI: 10.1063/1.4726110.

[59]   Davarpanah, A.; Belo, J. H.; Amaral, V. S.; Amaral, J. S. On the Optimization of Magneto-Volume Coupling for Practical Applied Field Magnetic Refrigeration. *physica status solidi (b)*. **2018**, *256* (3). DOI: 10.1002/pssb.201800419.

[60] X. B. Liu, Z. Altounian, D. H. Ryan, Structure and magnetic transition of LaFe13−xSix compounds, *J. Phys.: Condens. Matter.,* 15, (2003) 7385–7394, https://doi.org/10.1088/0953-8984/15/43/020

[61] Jicheng Feng, Ruben Geutjens, Nguyen V. Thang, Junjie Li, Xiaoai Guo, Albert Kéri, Shibabrata Basak, Gábor Galbács, George Biskos, Hermann Nirschl, Henny W. Zandbergen, Ekkes Brück, Andreas Schmidt-Ott, Magnetic Phase Transition in Spark-Produced Ternary LaFeSi Nanoalloys, *ACS Appl. Mater. Interfaces*, 10, 7, 6073–6078, 2018, https://doi.org/10.1021/acsami.7b15441

[62] C. O. Amorim, F. Mohseni, R. K. Dumas, V. S. Amaral, J. S. Amaral, A geometry-independent moment correction method for the MPMS3 SQUID-based magnetometer, *Measurement Science and Technology,* 32, 105602, 2021, https://doi.org/10.1088/1361-6501/ac0d23

[63] Henrique N. Beza, Kaspar K. Nielsen, Poul Norby, Anders Smith, Christian R. H. Bahl,

Magneto-elastic coupling in La(Fe, Mn, Si)13Hy within the Bean-Rodbell model, AIP Advances 6, 056217 (2016), https://doi.org/10.1063/1.4944400

[64] L. Jia, J. R. Sun, H. W. Zhang, F. X. Hu, C. Dong, B. G. Shen, Magnetovolume effect in intermetallics LaFe13−xSix, J. Phys.: Condens. Matter.,18, 9999, 2006, https://doi.org/10.1088/0953-8984/18/44/002

[65] S.Elomari, M. D. Skibo, A. Sundarrajan, H. Richards, Thermal expansion behavior of particulate metal-matrix composites, *Composites Science and Technology*, Volume 58, Issues 3–4, Pages 369-376, 1998, https://doi.org/10.1016/S0266-3538(97)00124-3

[66] YiWu Yan, Lin Geng, Effects of particle size on the thermal expansion behavior of SiCp/Al composites, *Journal of Materials Science*, volume 42, pages 6433–6438 (2007), https://doi.org/10.1007/s10853-006-1200-7

[67] J.González-Benito, E.Castillo, J. F.Caldito, Coefficient of thermal expansion of TiO2 filled EVA based nanocomposites. A new insight about the influence of filler particle size in composites, *European Polymer Journal,* Volume 49, Issue 7, Pages 1747-1752, 2013, https://doi.org/10.1016/j.eurpolymj.2013.04.023

[68] Jae-Soon Jang, Benoît Bouveret, Jonghwan Suhr, Ronald F. Gibson, Combined numerical/experimental investigation of particle diameter and interphase effects on coefficient of thermal expansion and young's modulus of SiO2/epoxy nanocomposites, *Polymer Composites,* 1416, 2012, https://doi.org/10.1002/pc.22268

SUPPLEMENTARY INFORMATION

Tailoring negative thermal expansion via tunable induced strain in La-Fe-Si-based multifunctional material

Rafael Oliveira Fleming*, Sofia Gonçalves*, Amin Davarpanah, Iliya Radulov, Lukas Pfeuffer, Benedikt Beckmann, Konstantin Skokov, Yang Ren, Tianyi Li, John Evans, Joao Amaral, Rafael Almeida, Armandina Lopes, Gonçalo Oliveira, João Pedro Araújo, Arlete Apolinário, João Horta Belo⧫

both authors contributed equally to this work
⧫ corresponding author e-mail: jbelo@fc.up.pt
R. O. Fleming*, S. Gonçalves*, A. Lopes, G. Oliveira, R. Almeida, J. P. Araújo, A. Apolinário and J. H. Belo⧫
Institute of Physics of Advanced Materials, Nanotechnology and Nanophotonics (IFIMUP), Departamento de Física e Astronomia da Faculdade de Ciências da Universidade do Porto, Rua do Campo Alegre, 687, 4169-007 Porto, Portugal

A. Davarpanah, I. Radulov, L. Pfeuffer, B. Beckmann, K. Skokov,
Institute of Material Science, Technical University of Darmstadt, 64287 Darmstadt, Germany

Y. Ren
Department of Physics, City University of Hong Kong, Kowloon, Hong Kong, China

T. Y. Li
X-ray Science Division, Argonne National Laboratory, Lemont, IL 60439, USA

A. Davarpanah, J. Amaral
Department of Physics and CICECO, University of Aveiro, Universitary Campus of Santiago, 3810-193 Aveiro, Portugal

J. S. O. Evans
Department of Chemistry, Durham University, South Road, Durham DH1 3LE, United Kingdom

Figure S1. NaZn13-type crystal structure (space group Fm-3c) of $LaFe_{11.9}Mn_{0.27}Si_{1.29}H_x$ compounds. Mn atoms tend to occupy both Fe(I) and Fe(II) sites and hydrogen atoms are located in interstitial sites within the unit cell.
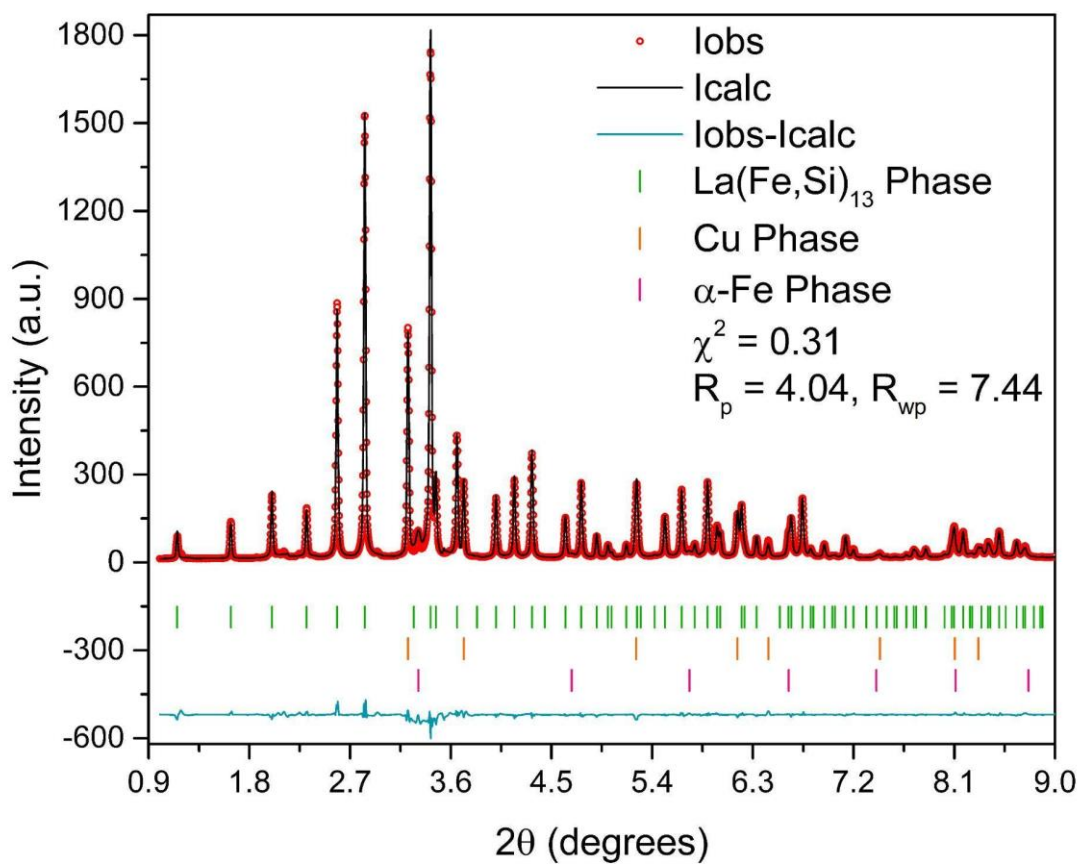
Figure S2. X-Ray diffractogram of sample BM14 performed at 273.55 K where a second phase of Fe is visible due to a small amount of α-Fe present in the sample and a cubic Cu phase is also visible due to the sample holder. All the diffractograms were measured using synchrotron radiation ($\lambda = 0.1173$ Å).
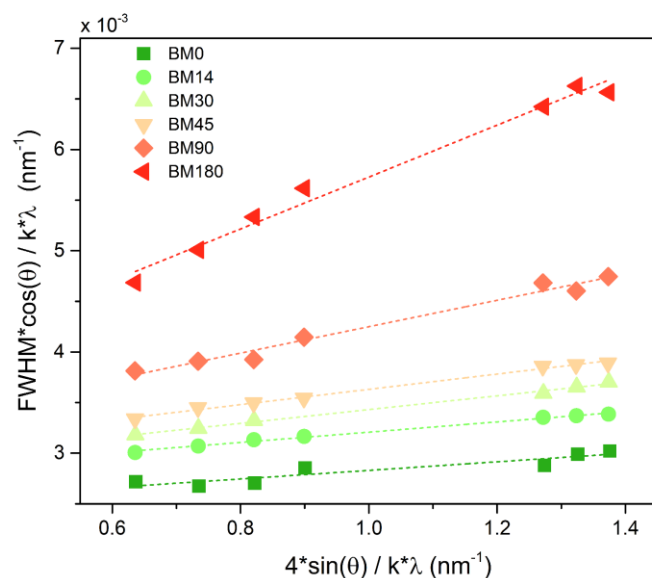
Figure S3. Williamson-Hall analysis of $LaFe_{11.9}Mn_{0.27}Si_{1.29}H_x$ diffracted peaks from all the samples diffractograms measured at 333 K.

$$\frac{dM}{dT}_{peak} = 0.215 * \exp\left(-\frac{t_{BM}}{20.56}\right) + 0.016$$
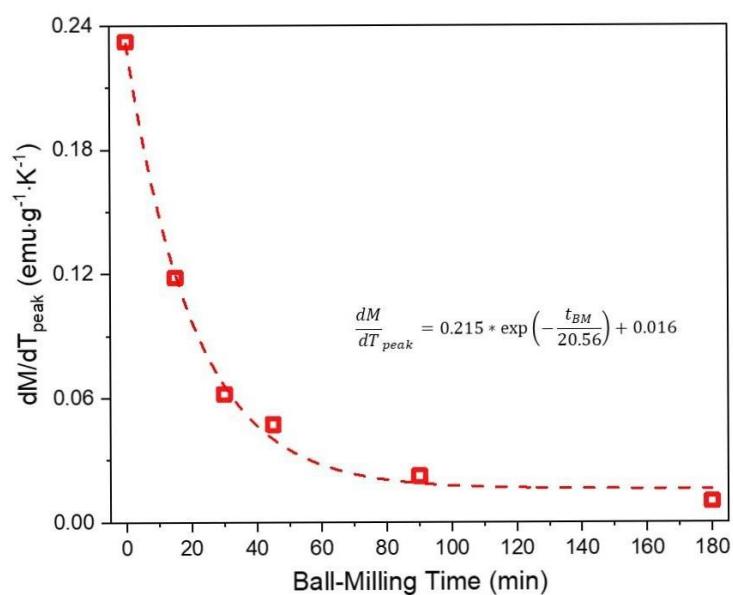
Figure S4. dM/dT ($T = 250\ K$) peak height of $LaFe_{11.9}Mn_{0.27}Si_{1.29}H_x$ samples as a function of ball-milling time.
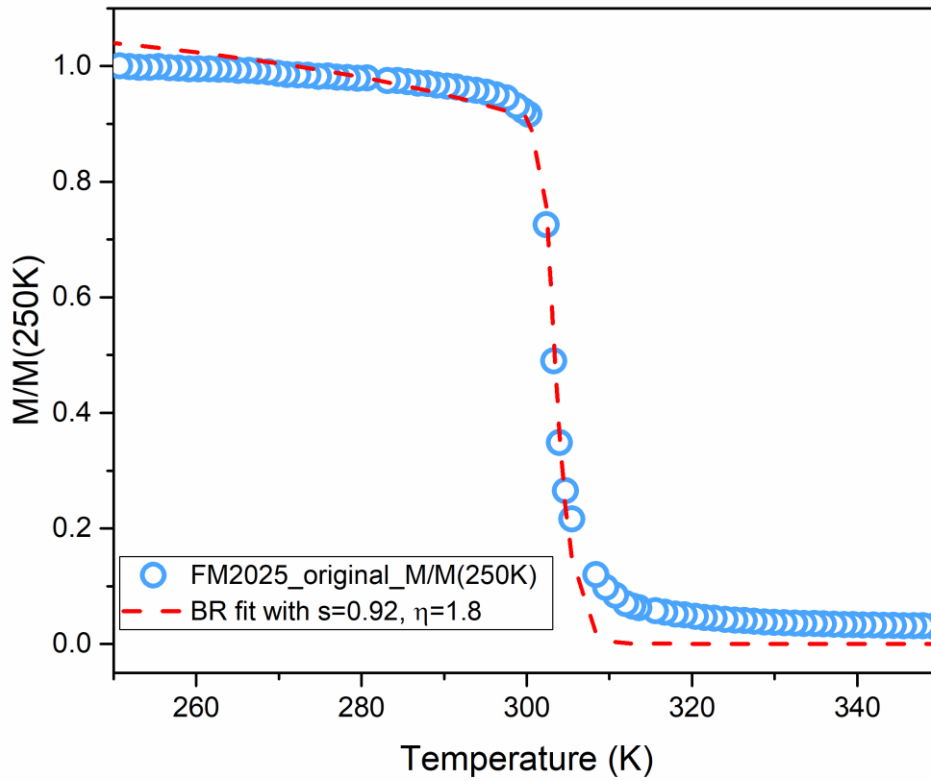
Figure S5. Bean-Rodbell fit to the $M/M_{T=250K}$ of the as-prepared sample of LaFe$_{11.9}$Mn$_{0.27}$Si$_{1.29}$H$_x$, assumed fixed values for spin (0.92) and η (1.8).
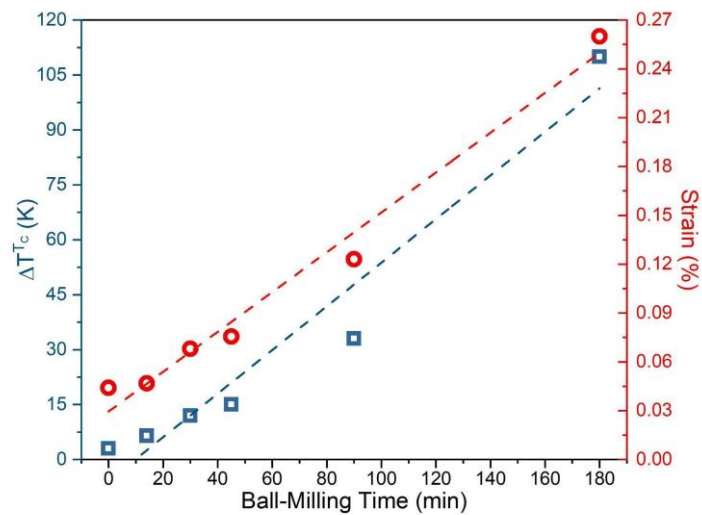

Figura S6. ΔT^{T_C} ($slope = 0.59558 \pm 0.06882$) (blue squares) and strain (%) ($slope = 0.00122 \pm 9.767 \times 10^{-5}$) (red circles) as a function of ball-milling time.
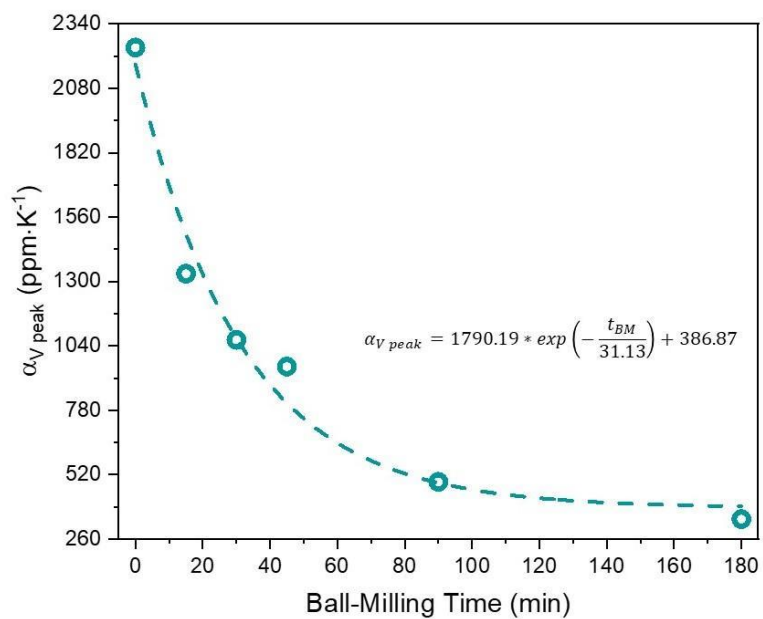
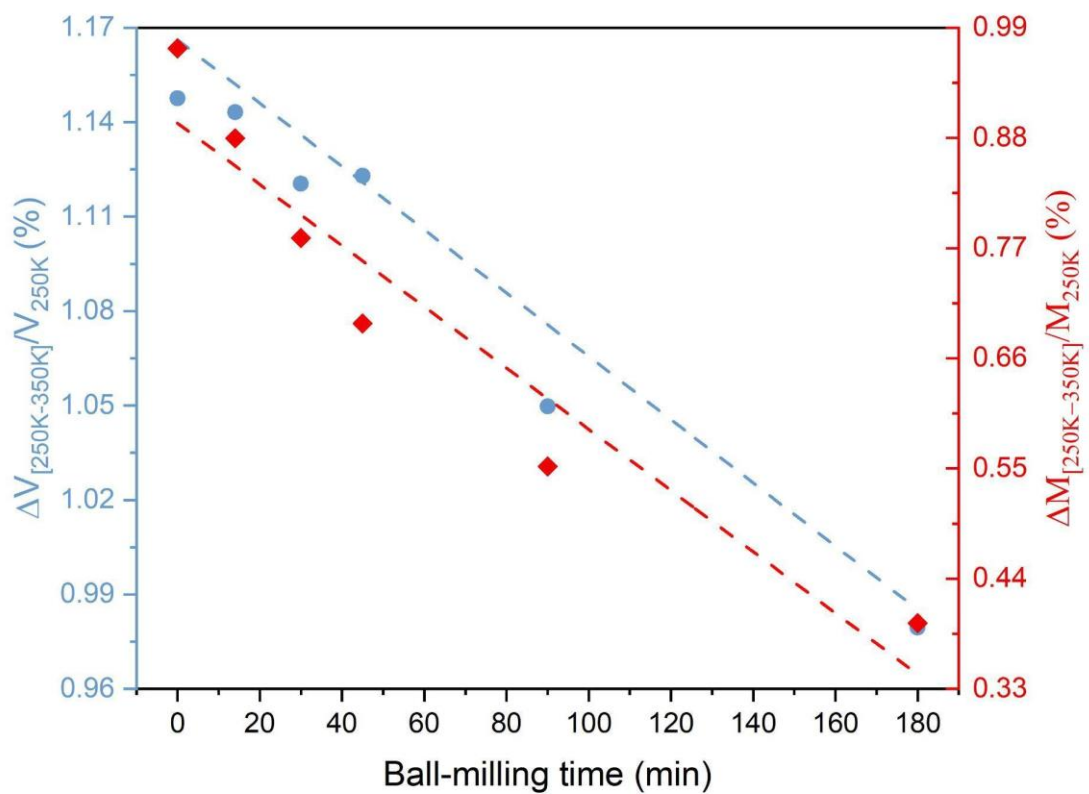**Figure S7.** $\alpha_V(T)_{peak}$ as a function of ball-milling time with corresponding exponential fit.

The equation shown in the figure:

$$\alpha_{V\ peak} = 1790.19 * exp\left(-\frac{t_{BM}}{31.13}\right) + 386.87$$
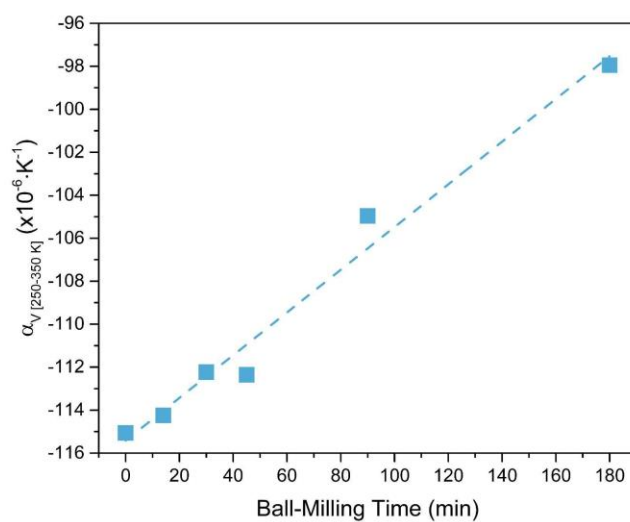
Figure S8. $\underline{\alpha}_{V\ [250-350\ K]}$ in the temperature range from 250 to 350 K as a function of ball-milling time.
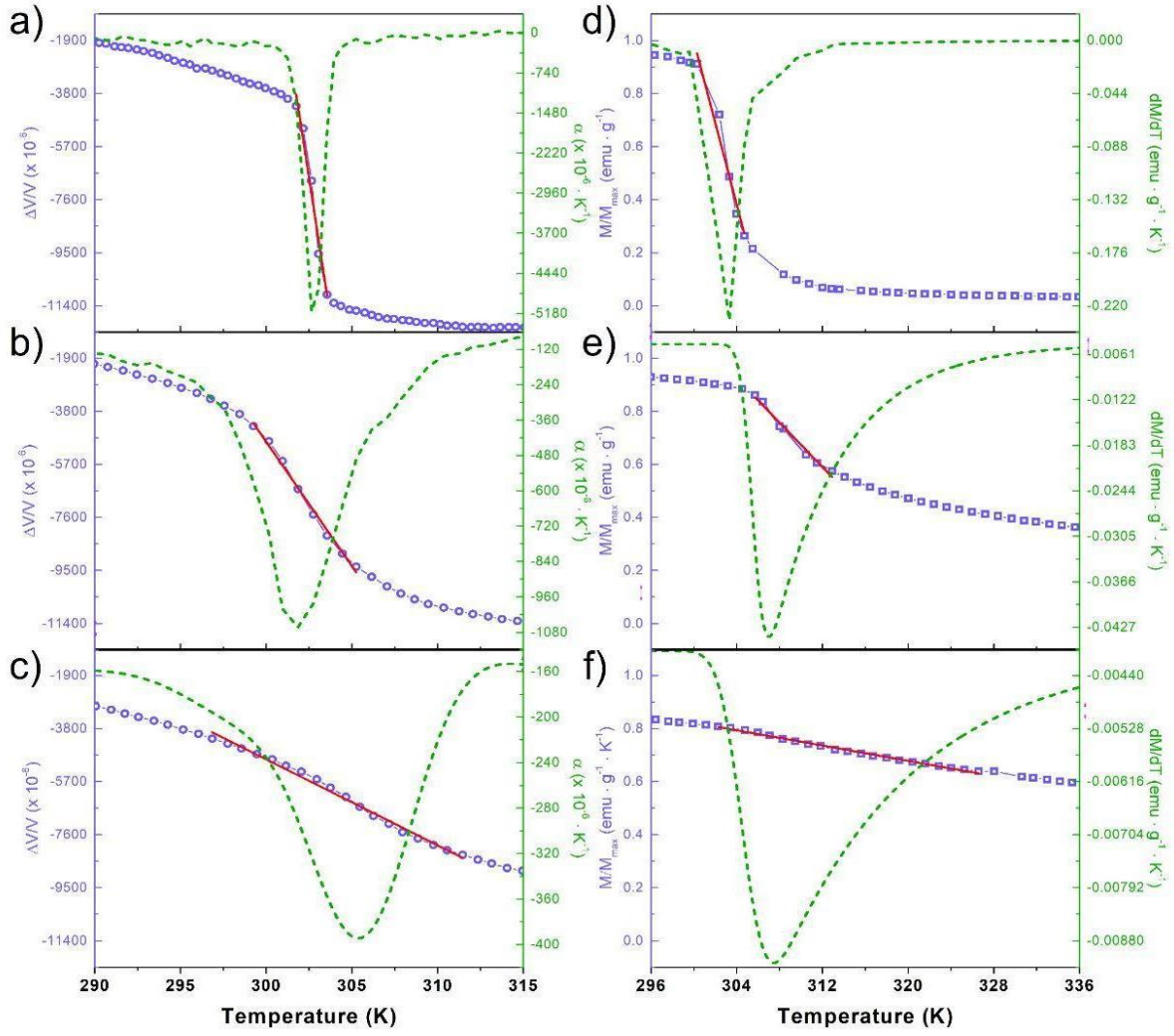
Figure S9. $\Delta V/V(T)$ (T=250 K) (blue cicles), $\alpha_V(T)(= \frac{d(\Delta V/V)}{dT})$ (green dash line) and the slope of the $\Delta V/V(T)$ analyzed at the FWHM of the $\alpha_V(T)$ curve (red line), $\underline{\alpha}_V$, for the samples a) as-prepared, b) BM45 and c) BM180. $M/M_{T=250K}$ (blue squares), dM/dT ($T = 250\ K$) (green dash line) and the slope of the $M/M_{T=250K}$ analyzed at the FWHM of the dM/dT ($T = 250\ K$) curve (red line), for the samples a) as-prepared, b) BM45 and c) BM180.

Figure S10. Relative percentual volume and magnetization change between 250K and 350K as a function of ball-milling time.
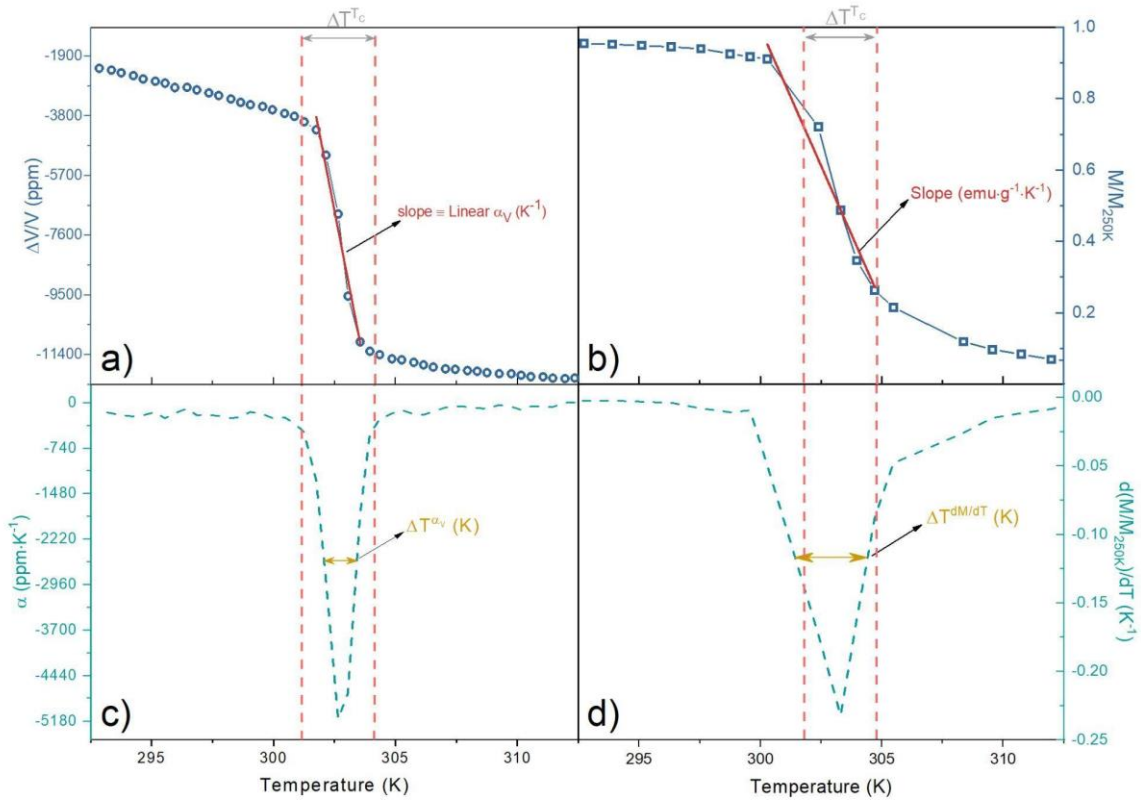
Figure S11. a) $\Delta V/V(T)$ and b) $M/M_{max}(T)$ with respective derivatives c) $\alpha(T)$, and d) $dM/dT(T)$, of the as-prepared sample. Schematic figure meant to show the temperature intervals ($\Delta T^{\alpha_V}, \Delta T^{dM/dT}, \Delta T^{T_C}$) and slopes referenced throughout the paper. The red dashes represent the temperature interval ΔT^{T_C} calculated using the Williamson-Hall analysis around the samples' T_C.
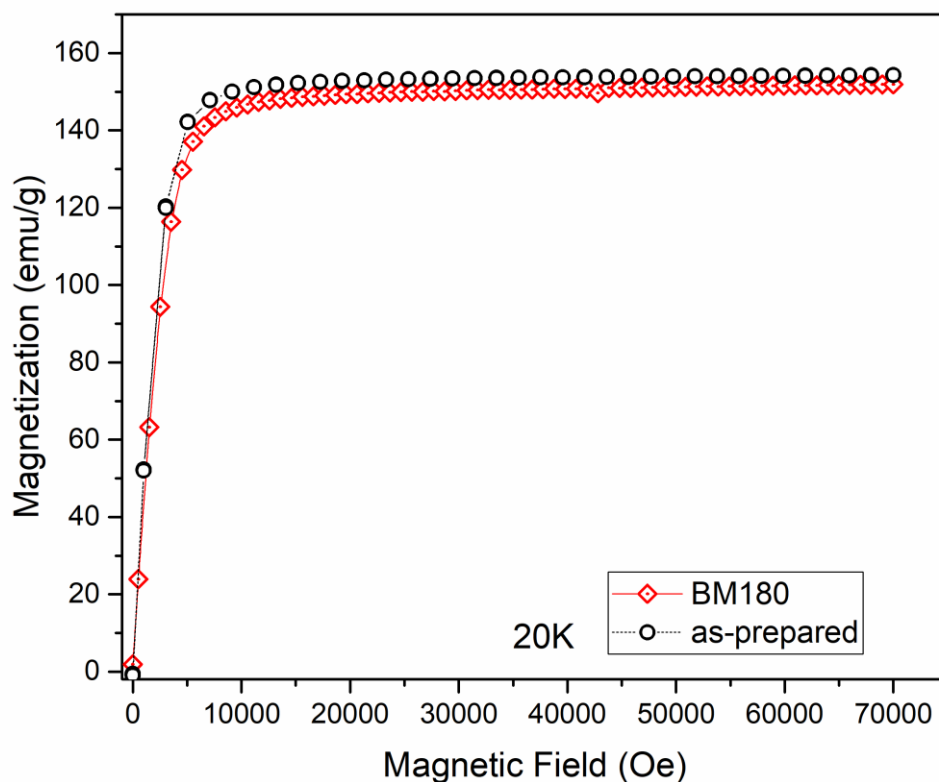
Figure S12. As-prepared and ball-milled for 180 minutes samples magnetization versus magnetic field curves measured at 20K.
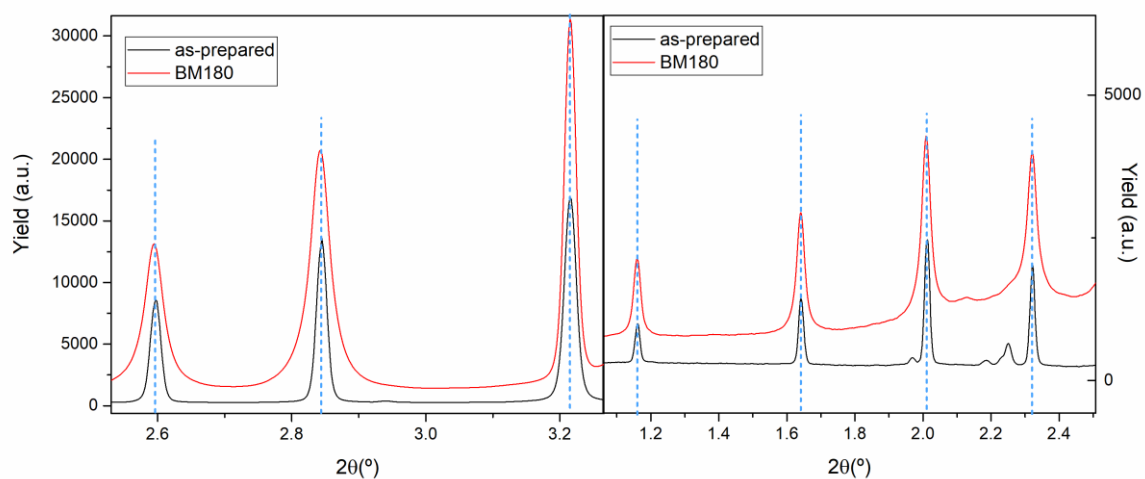
Figure S13. XRD pattern peaks of the as-prepared and ball-milled for 180 minutes samples, highlighting their identical center position.
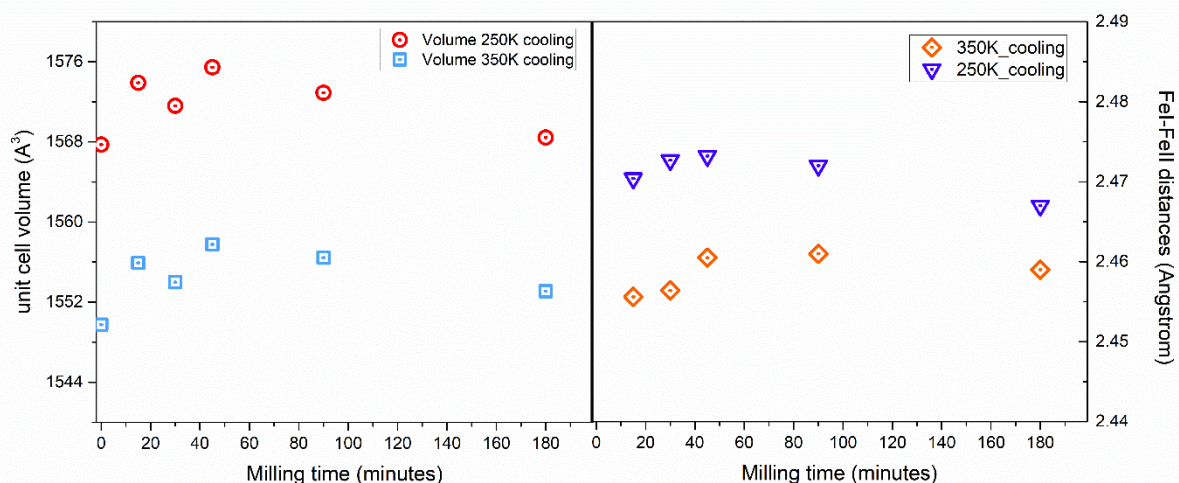
Figure S14. Unit cell volume (left-hand) and FeI-FeII interatomic distances (right-hand) obtained from the Rietveld refinements of the XRD patterns measured at low (250K) and high temperature (350K) regions as a function of ball milling time.
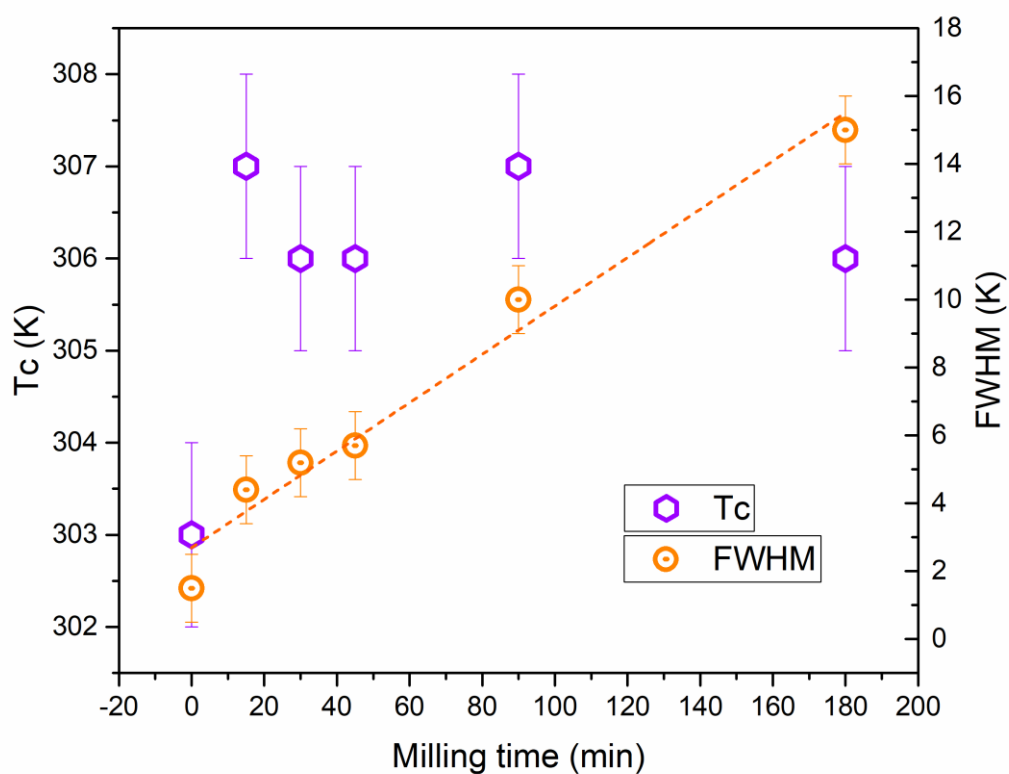
Figure S15. The magnetic transition temperature (Tc, left-axis) and the full width at half maximum of the dM/dT peak (at Tc) as a function of ball milling time.